Investigation on the energy performance of using air-source heat pump to charge PCM storage tank

Yantong Li[a,b,*], Nan Zhang[b], Zhixiong Ding[c]

[a]Department of Architecture and Civil Engineering, City University of Hong Kong, Tat Chee Avenue, Kowloon, Hong Kong, China

[b]Department of Energy and Process Technology, Norwegian University of Science and Technology, Kolbjørn Hejes vei 1 B, Trondheim 7491, Norway

[c]School of Energy and Environment, City University of Hong Kong, Tat Chee Avenue, Kowloon, Hong Kong, China

*Corresponding author; Tele: 852-56100432; 86-14714316174; Email: yantong.li@ntnu.no

Abstract

Nowadays air-source heat pumps are widely used to collect heat from ambient air, which can reduce operating cost and protect environment when compared with fossil-based heating systems. To increase the flexibility of heat collection and supply, air-source heat pump should be used together with a thermal storage tank. In this heating system, air-source heat pump needs to charge the storage tank regularly based on a predefined time schedule. When a PCM storage tank is used, the charging completion time and the total energy use are nonlinearly relative to the charging water flow rate. This study, therefore, systematically investigates the relationships between the charge water flowrate and the charging completion time and the total energy use. These relationships are analyzed qualitatively and then evaluated quantitatively using case studies, according to which optimal water flow rate is identified.

Keywords: PCM storage tank; thermal energy storage; charging performance; air-source heat pump

1. Introduction

Energy is a critical concern in the development of society nowadays [1, 2]. Fossil fuels are still the major source for satisfying the energy demand although they lead to environmental pollution problems, such as global warming and desertification [3-6]. To alleviate pollutions, renewable energy harvest has gained fast development recently in many countries [7, 8]. For example, European Union (EU) states that by 2020 the utilization of renewable energy should account for 20% of the total energy consumption [9]. As one of renewable energy harvest technologies, an air-source heat pump collects heats directly from ambient air with high efficiency (even in cold seasons). Due to its low initial cost, simple structure, and environmentally friendly feature [10], it has been widely used in space heating [11] and hot water generation [12].

In many applications, an air-source heat pump should be used together with a heat storage tank in order to overcome the mismatch between the energy supply and the heat demand or reduce the operating cost by shifting the charging from electrical on-peak hours to off-peak hours [13, 14], although it will cause the heat energy loss when a storage tank is utilized. Because phase change materials (PCMs) have many advantages in heat storage, such as high energy storage density and nearly isothermal temperature during the phase change process [15-18], the use of PCMs in a storage tank has gained popularity, which can efficiently reduce the volume of the storage tank or increase the amount of heat stored in the tank [19-22]. For example, Zou et al. [19] showed that PCMs was able to effectively reduce the volume of heating storage tanks when it was used in a heating system. Kumar et al. [23] found that the stratification capability of PCM storage tanks was stronger than that of water tanks. Navarro et al. [16] reported that the energy efficiency of a domestic hot water system with a PCM storage tank was enhanced when compared with that with water tank. Moreno et al. [24] compared with the space cooling system with water tank and PCM storage tank. It was concluded that the PCM storage tank can supply 14.5% more cold energy than the water tank.

The investigations for the charging performance of PCM storage tanks are a research hotspot, which has attracted scholars' attentions. For instance, Wang et al. [25] evaluated the charging performance of a solar heat storage system with a PCM storage tank in different mass flow rate and solar collecting area. They concluded that the mass flow rate had the little influence on the thermal performance of the system, and the solar collecting area had important influence on that. Yang et al. [26] presented the energy and exergy analysis for the charging performance of the solar storage system with multiple-type packed bed PCM storage tank. They found that the energy and exergy efficiencies of the multiple-type packed bed PCM storage tank were higher than those of the single-type packed bed PCM storage tank. Elbahjaoui and Qarnia [27] compared the charging performance of the solar storage system with double concentric-tube and triple concentric-tube PCM storage tank. They found that the storage efficiency of the former one was lower than that of the latter one. Moreno et al. [24] compared the charging performance of the cooling system with the water tank and PCM storage tank. It was concluded that the charging time of the system with the PCM storage tank was 4.55 times higher than that of the system with the water tank. Cheng and Zhai [28] compared the charging performance of the chilled-water storage system with three-stage cascaded and single-stage PCM storage tank. They concluded that the cold charging rate of the system with the three-stage cascaded PCM storage tank was 11%-35% higher than that of the system with single-stage PCM storage tank. However, a systematic investigation for using air-source heat pumps to charge PCM storage tank is lacking.

The use of PCMs, however, makes the charging a nonlinear process. During the charging procedure, an air-source heat pump and its associated PCM storage tank form a closed loop, connected by cycling water driven by a water pump. The heat pump collects heat from ambient air, transferring the heat to the cycling water. The cycling water delivers the heat to the tank, transferring the heat to the phase changing materials and the water inside the tank. In this process, the tank temperature will increase in a nonlinear manner due to the use of PCM: it increases quickly before and after the phase change; but slowly during the phase change. The air-source heat pump will experience from full load to partial load condition: it works under full load condition at the beginning of charging; but approaches to very partial load condition near the end of charging. Due to the dynamic operating condition, the COP and the power of the air-source heat pump may change significantly.

To study the dynamic behavior of the charging process, an important issue to be concerned is the charging speed. Generally, charging should be completed as fast as possible. The charging speed is affected by many factors, for example the thermal properties of PCM materials and the configuration of PCM storage tanks [29, 30]. Given the PCM material and the configuration of the tank, the charging speed have a strong relationship with the cycling water flowrate. Wu et al.'s study [31] showed that when the cycling water flowrate was reduced from 50 L/min to 10 L/min, the charging completion time was increased from 41 min to 535 min, increasing by nearly 13 times. Another important issue is the energy use of the air-source heat pump during the charging process. Indeed, charging should be completed with the lowest energy use without sacrificing the charging speed. However, this issue has not been comprehensively studied until now.

This paper therefore proposes a comprehensive study to investigate the energy performance of the charging process when an air-source heat pump is used to change a PCM storage tank, aiming to provide a guideline for optimizing the operation of such a heat collection system regarding to energy use. To this end, a heat collection system of an air-source heat pump with PCM storage tank is considered. A simulation platform will be constructed using MATLAB and TRNSYS. A test rig will be set up to validate the model of the air-source heat pump that is used in the simulation platform. Based on the validated simulation platform, the energy performance of the system during the charging process will be investigated under different cycling water flowrates. The relationship between the energy consumption and the cycling water flowrate will be analyzed, and the optimal flowrate that lead to the minimum energy use will be identified. The rest of the paper is organized as follows: Section 2 describes the proposed methodology for studying the charging performance of PCM storage tank. Section 3 shows the case study. Results and analysis are shown in Section 4. Concluding remarks are summarized in Section 5.

2. Methodology

2.1. System description

The schematic diagram of the system to be investigated in this study is shown in Fig. 1 (a). The main components include a PCM storage tank, an air-source heat pump, and a water pump. The air-source heat pump composes of expansion valve, condenser, evaporator, and compressor. As shown in Fig. 1 (b), two performance indices are concerned in the charging process. One is the charging completion time, and another is the total energy use. Both of them are affected by outdoor air temperature and the cycling water flowrate, and thus the outdoor air temperature and the cycling water flowrate are considered as two critical variables of the charging process. It should be noted that the cycling water flowrate of the water pump can be adjusted by the inverter in this system.

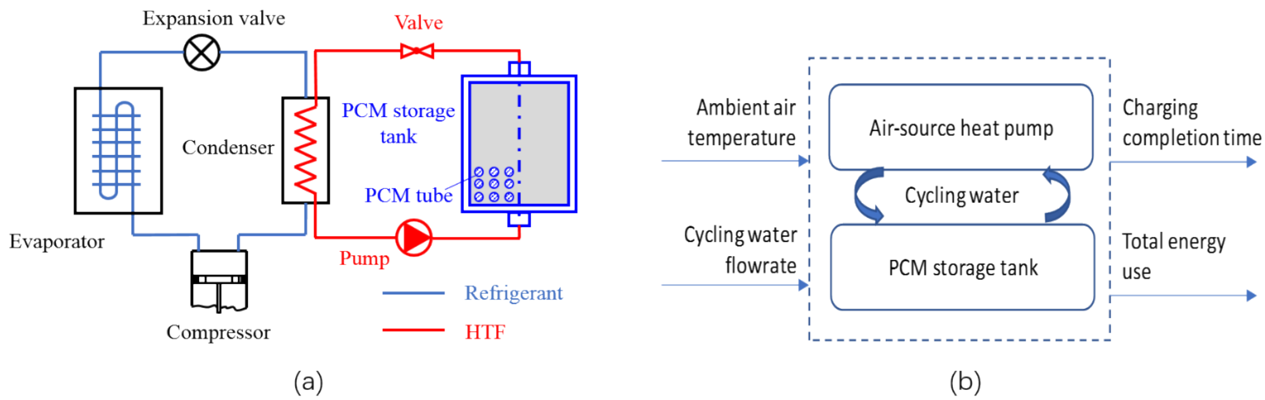

Fig. 1. (a) Schematic diagram of the heat collection and storage system; and (b) decision variables and performance indices for the charging process.

The charging completion time is the time needed to finish the charging, which is strongly relative to the water flowrate $(\dot{m}_w)$, as described by:

$$t_c = t_1 - t_0 = f(\dot{m}_w, T_{amb}) \tag{1}$$

where t_0 is the charging start time, and t_1 is the charging finish time. Generally, charging can be finished faster if the cycling water flowrate is larger or/and ambient air temperature is higher.

In this heat collection system, electricity is needed for the air-source heat pump and the water pump during the charging process. The total energy use E_{total} is:

$$E_{total} = E_{ashp} + E_{wp} \tag{2}$$

where the energy use of the water pump is given by:

$$E_{wp} = \int_{t_0}^{t_1} P_{wp} dt \tag{3}$$

If a constant speed water pump is used, the water pump power P_{wp} is relatively stable and the energy use of the pump is proportional to the charging completion time t_c $(= t_1 - t_0)$. Certainly, the water pump has a higher power when the cycling water flowrate is larger, which can be shown by an empirical pump model [32]:

$$\frac{P_a}{P_d} = c0 + c1\frac{\dot{m}_{fc}}{\dot{m}_{f0}} + c2\left(\frac{\dot{m}_{fc}}{\dot{m}_{f0}}\right)^2 + c_3\left(\frac{\dot{m}_{fc}}{\dot{m}_{f0}}\right)^3 \tag{4}$$

where $\dot{m}_{fc}$ and $\dot{m}_{f0}$ are the actual and design mass flowrate; and P_a and P_d are the actual and designed power; and c is a coefficient which can be identified using field data. However, the energy use of the water pump during the charging process may not be higher since the charging completion time will be shorter with a higher cycling water flowrate.

The energy use of the air-source heat pump can be written as:

$$E_{ashp} = \int_{t_0}^{t_1} [P_{ashp}(t) + P_{fan}(t)]dt \quad (5)$$

where P_{fan} is the fan power, which is relatively constant when a constant speed fan is used; and P_{ashp} is the compressor power of the heat pump, which should not be a constant during the charging process. The compressor power is related to the ambient air temperature T_{amb} and the inlet water temperature T_{in} [33]:

$$P_{ashp} = f(T_{amb}, T_{in}) \quad (6)$$

During the charging process, the ambient air temperature should be relative stable (the charging process can be normally finished in two or three hours); while the inlet water temperature increases gradually with the charging process. This indicates that the heat pump will experience from full load operating condition (at the beginning) and very partial load operating condition (near the end) and therefore the variation of the power P_{ashp} should be nonlinear with the charging time. This nonlinearity becomes worse when PCM is used. This is because the water temperature increases at the phase changing stage should be slower compared with the temperature increase before and after the phase changing stage. As the water flow rate will affect both the charging completion time, different water flow rate may lead to different energy use of the heat pump in a single charging process.

2.2. Methodology to analyze the charging performance

The proposed study in this paper aims to investigate systematically how the cycling charging water flowrate affects the concerned charging performance (charging completion time and total energy use). Fig. 2 shows the research methodology used in this study. Firstly, a simulation platform will be constructed using TRNSYS and MATLAB, which includes the models of the air-source heat pump and the PCM storage tank as well as weather data. Before carrying out the simulation study, the models of the air-source heat pump and the PCM storage tank will be validated using the data collected from experiments. Secondly, after specifying the charging target (i.e. the maximum outlet temperature of the air-source heat pump is raised to be, say, 55 ^{o}C), the effect of different cycling water flowrate on the charging completion time and the total energy use will be analyzed using the data generated from the simulation platform. Finally, the relationship between the cycling water flowrate and different evaluation indicators will be established to identify the optimal flowrate.

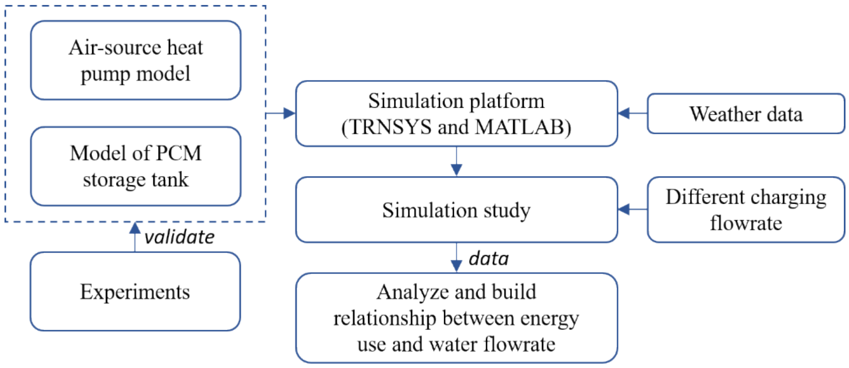

Fig. 2. The research methodology used in this study.

2.3. Component models

2.3.1. Air-source heat pump model

To develop the air-source heat pump model in TRNSYS, it is important to develop the correction-factors table that includes the correction factors of power and heat transfer rate in different ambient temperature and inlet water temperature. The steady-state model in MATLAB will be adopted to identify the correction factors in different water mass flow rate, shown in Fig. 3. The input variables of the model in MATLAB include water mass flow rate, ambient temperature, inlet water temperature, and structural parameters of air-source heat pump. The REFPROP will be adopted to provide the thermal properties information of refrigerant for the model in MATLAB. The output variables of the model in MATLAB include power and heat transfer rate. It should be noted that the air-source heat pump model in TRNSYS (i.e. Type 941) is established in accordance with performance maps, which should be constructed by a mass of data. Current laboratory conditions are limited to obtain huge amount of accurate data in different water mass flow rate for completing performance maps. Hence, the method presented in Fig. 3 is applied to develop the air-source heat pump model in TRNSYS.

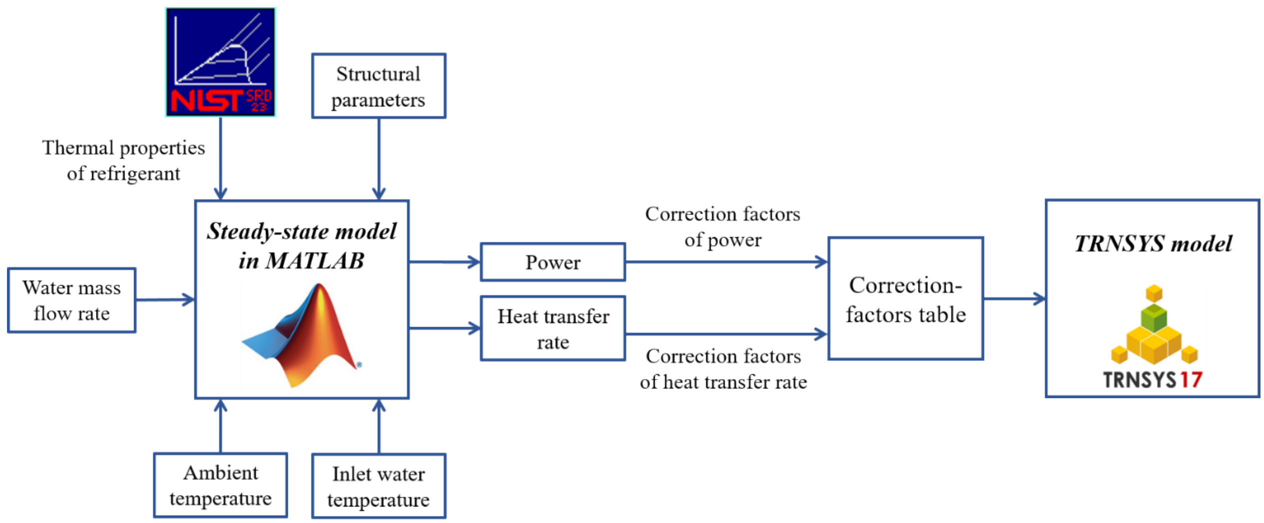

Fig. 3. Connection between steady-state model in MATLAB and model in TRNSYS.

(a) Steady-state model in MATLAB

The steady-state model of the air-source heat pump is established by the integration of sub-models of main components including compressor, expansion valve, evaporator and condenser. Fig. 4 depicts the typical T-s and P-h diagram of the vapor compression refrigeration cycle. The model is adopted to simulate the heat transfer process in the air-source heat pump, which is based on several assumptions: (1) The isenthalpic process occurs in the expansion valve; (2) The isentropic process occurs in the compressor; (3) The degree of superheat of the evaporator is assumed to be 2^{o}C [34]; and (4) there is no pressure drop for the refrigerant in the evaporator and condenser. The sub-models of main components are depicted as follows.

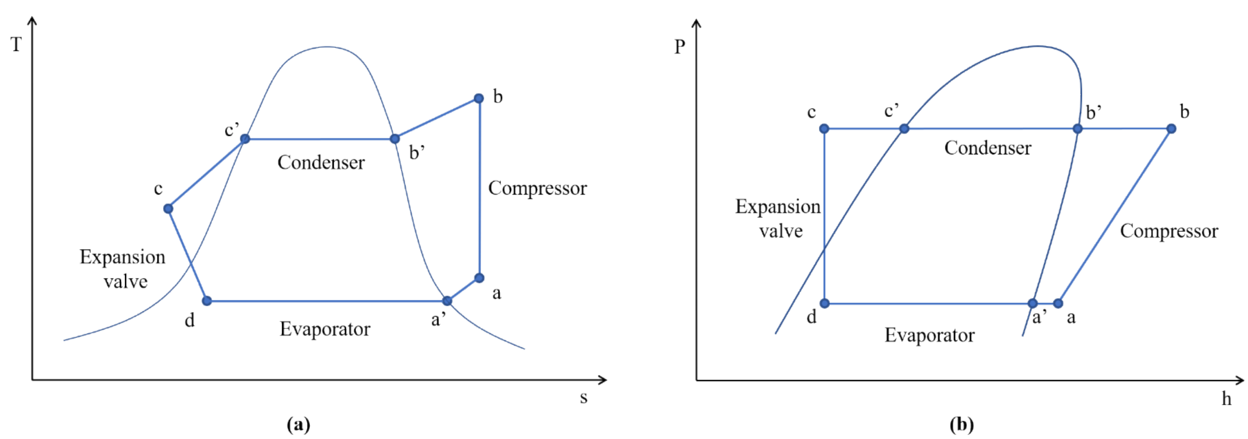

Fig. 4. Typical (a) T-s and (b) P-h diagram of the vapor compression refrigeration cycle.

- Compressor

The mathematical model of the compressor is constructed to identify the mass flow rate of the refrigerant and consumed power. The mass flow rate of the refrigerant in the compressor (m_c) is calculated by Eqn. (7) [35]:

$$m_c = \frac{n_c V_c \eta_{cv}}{60 v_c} \tag{7}$$

where n_c is the rotational velocity; V_c is the displacement volume; η_{cv} is the compressor volumetric efficiency; and v_c is the gas specific volume at the suction port. The consumed power of the compressor (W_c) is calculated by Eqn. (8):

$$W_c = m_c(h_d - h_s)/\eta_{ci} \tag{8}$$

where η_{ci} is the isentropic efficiency; and h_d and h_s are the discharging and suction enthalpy, respectively.

- Condenser

The heat transfer process in the refrigerant side of the condenser can be expressed by Eqn. (9):

$$Q_{c,r} = m_{cn}(h_{i,c} - h_{o,c}) \tag{9}$$

where $Q_{c,r}$ is the heat transfer rate in the refrigerant side of the condenser; m_{cn} is the mass flow rate of the refrigerant in the condenser; $h_{i,c}$ and $h_{o,c}$ are the inlet and outlet enthalpy of the refrigerant in the condenser, respectively.

The heat transfer process in the water side of the evaporator can be expressed by Eqn. (10):

$$Q_{c,w} = m_w c_w (T_{o,w} - T_{i,w}) \tag{10}$$

where $Q_{c,w}$ is the heat transfer rate in the water side of the evaporator; m_w is the mass flow rate of the water; c_w is the specific heat of the water; and $T_{o,w}$ and $T_{i,w}$ are the outlet and inlet temperature of the water, respectively.

The heat transfer process between the refrigerant and the water in the condenser can be expressed by Eqn. (11):

$$Q_c = U_c A_c \Delta T_c \tag{11}$$

where Q_c is the heat transfer rate between the water and the refrigerant in the condenser; U_c is the total heat transfer coefficient of the condenser; ΔT_c is the log-mean temperature difference of the condenser.

The total heat transfer coefficient of the condenser (U_c) is calculated by Eqn. (12):

$$U_c = \frac{1}{\frac{1}{h_c} + \frac{1}{h_w}} \tag{12}$$

where h_c and h_w are the heat transfer coefficient of the refrigerant and the water in the condenser, respectively.

The log-mean temperature difference of the evaporator (ΔT_c) is calculated by Eqn. (13):

$$\Delta T_c = \frac{\Delta T_{c,1} - \Delta T_{c,2}}{ln\frac{\Delta T_{c,1}}{\Delta T_{c,2}}} \tag{13}$$

where $\Delta T_{c,1}$ and $\Delta T_{c,2}$ are the temperature difference in the one side and another side of the condenser, respectively.

The heat transfer coefficient in the water side can be calculated by Eqn. (14):

$$h_w = \frac{k_{wr} Nu_{wc}}{D_c} \tag{14}$$

where D_c is the hydraulic diameter. The Nu_{wc} is calculated by the Eqn. (15) [36]:

$$Nu_{wc} = C_{wc}(Re_{wc})^{wn}(Pr_{wc})^{\frac{1}{3}}(\frac{\mu_{wc}}{\mu_{wcw}})^{0.17} \tag{15}$$

where Re_{wc} and Pr_{wc} are the Reynolds number and Prandtl number of the water in the condenser, respectively; μ_{wc} is the viscosity of the water; μ_{wcw} is the viscosity of the water in the wall temperature; and C_{wc} and wn are two coefficients.

The coefficient C_{wc} is calculated by Eqn. (16):

$$C_{wc} = \begin{cases} 0.718 & Re_{wc} \leq 10 \\ 0.348 & Re_{wc} > 10 \end{cases} \tag{16}$$

The coefficient wn is calculated by Eqn. (17):

$$wn = \begin{cases} 0.349 & Re_{wc} \leq 10 \\ 0.663 & Re_{wc} > 10 \end{cases} \tag{17}$$

The heat transfer coefficient of the single-phase refrigerant in the condenser (h_{sc}) is calculated by Eqn. (18):

$$h_{sc} = \frac{k_{sc} Nu_{sc}}{D_c} \tag{18}$$

where k_{sc} is the thermal conductivity of the single-phase refrigerant in the condenser.

The heat transfer coefficient of the two-phase refrigerant in the condenser (h_{tc}) is calculated by Eqn. (19):

$$h_{tc} = \frac{k_{tc} Nu_{tc}}{D_c} \tag{19}$$

where k_{tc} is the thermal conductivity of the two-phase refrigerant in the condenser. The Nu_{tc} is calculated by Eqn. (20) [37]:

$$Nu_{tc} = 0.0125\left(Re_{tc}\sqrt{\frac{\rho_{cl}}{\rho_{cv}}}\right)^{0.9}\left(\frac{x_c}{1 - x_c}\right)^{0.1x_c + 0.8} Pr_{cl}^{0.63} \tag{20}$$

where Re_{tc} is the Reynolds number of the two-phase refrigerant in the condenser; ρ_{cl} and ρ_{cv} are the density of the liquid-phase and vapor-phase refrigerant in the condenser, respectively; x_c is the vapor quality in the condenser; and Pr_{cl} is the Prandtl number of the liquid-phase refrigerant in the condenser.

- Expansion valve

The mathematical model of the expansion valve is constructed to identify the mass flow rate (m_v), which is calculated by Eqn. (21) [38]:

$$m_v = A_v C_v \sqrt{2\rho_i (P_i - P_o)} \tag{21}$$

where A_v is the cross-section area; ρ_i is the inlet density; P_i and P_o are respectively the inlet and outlet pressure; C_v is the flow coefficient of the expansion valve, which is calculated by Eqn. (22) [39]:

$$C_v = 0.02005\sqrt{\rho_i} + 0.634 v_o \tag{22}$$

where v_o is the outlet specific volume.

- Evaporator

The heat transfer process in the refrigerant side of the evaporator can be expressed by Eqn. (23):

$$Q_{e,r} = m_e(h_{o,e} - h_{i,e}) \tag{23}$$

where $Q_{e,r}$ is the heat transfer rate in the refrigerant side of the evaporator; m_e is the mass flow rate of the refrigerant in the evaporator; $h_{o,e}$ and $h_{i,e}$ are the outlet and inlet enthalpy of the refrigerant in the evaporator, respectively.

The heat transfer process in the air side of the evaporator can be expressed by Eqn. (24):

$$Q_{e,a} = m_a c_a(T_{i,a} - T_{o,a}) \tag{24}$$

where $Q_{e,a}$ is the heat transfer rate in the air side of the evaporator; m_a is the mass flow rate of the air; c_a is the specific heat of the air; and $T_{i,a}$ and $T_{o,a}$ are the inlet and outlet temperature of the air, respectively.

The heat transfer process between the refrigerant and the air in the evaporator can be expressed by Eqn. (25):

$$Q_e = U_e A_e \Delta T_e \tag{25}$$

where Q_e is the heat transfer rate between the air and the refrigerant in the evaporator; U_e is the total heat transfer coefficient of the evaporator; ΔT_e is the log-mean temperature difference of the evaporator.

The total heat transfer coefficient of the evaporator (U_e) is calculated by Eqn. (26):

$$U_e = \frac{1}{\frac{1}{h_e} + \frac{1}{h_a}} \tag{26}$$

where h_e and h_a are the heat transfer coefficient of the refrigerant and the air in the evaporator, respectively.

The log-mean temperature difference of the evaporator (ΔT_e) is calculated by Eqn. (27):

$$\Delta T_e = \frac{\Delta T_{e,1} - \Delta T_{e,2}}{ln\frac{\Delta T_{e,1}}{\Delta T_{e,2}}} \tag{27}$$

where $\Delta T_{e,1}$ and $\Delta T_{e,2}$ are the temperature difference in the one side and another side of the evaporator, respectively.

The heat transfer coefficient in the air side (h_a) can be calculated by Eqn. (28) [40]:

$$h_a = \frac{j_a \rho_a u_m c_a}{Pr_a^{2/3}} \tag{28}$$

where ρ_a is the density of the air; c_a is the specific heat of the air; j_a is the heat transmission factor; u_m is the maximum wind speed; and Pr_a is the Prandtl number of the air.

The heat transmission factor (j_a) is calculated by Eqn. (29):

$$j_a = 0.0014 + 0.2618 Re_a^{-0.4} \left(\frac{A_{af}}{A_a}\right)^{-0.15} \tag{29}$$

where Re_a is the Reynolds number; and A_{af} and A_a are the surface area of the tubes with and without fins, respectively.

The maximum wind speed (u_m) is calculated by Eqn. (30):

$$u_m = u_f \frac{s_h s_v}{(s_h - D_{te})(d_1 - d_2)} \tag{30}$$

where u_f is the wind speed of the fan; s_h and s_v are the tube spacings in the horizontal and vertical directions, respectively; D_{te} is the diameter of the tubes; and d_1 and d_2 are the thickness and spacing of the fins, respectively.

The heat transfer coefficient of the single-phase refrigerant in the evaporator (h_{se}) is calculated by Eqn. (31):

$$h_{se} = \frac{k_{se} Nu_{se}}{D_{te}} \tag{31}$$

where k_{se} is the thermal conductivity of the single-phase refrigerant in the evaporator. The Nu_{se} is calculated by Eqn. (32):

$$Nu_{se} = \frac{(f_{se}/8) Re_{se} Pr_{se}}{1.07 + 1.27\left(\frac{f_{se}}{8}\right)^{0.5} \left(Pr_{se}^{\frac{2}{3}} - 1\right)} \tag{32}$$

where Re_{se} and Pr_{se} are the Reynolds number and Prandtl number of the single-phase refrigerant in the evaporator; f_{se} is the friction coefficient, calculated by Eqn. (33):

$$f_{se} = (1.82 ln Re_{se} - 1.64)^{-2} \tag{33}$$

The heat transfer coefficient of the two-phase refrigerant in the evaporator (h_{te}) is calculated by Eqn. (34):

$$h_{te} = h_{el}\left\{\left[(1-x_e) + 1.2x_e^{0.4}(1-x_e)^{0.01}\left(\frac{\rho_{el}}{\rho_{ev}}\right)^{0.37}\right]^{-2.2} + \left[\frac{h_{ev}}{h_{el}}x_e^{0.01}\left(1+8(1-x_e)^{0.7}\left(\frac{\rho_{el}}{\rho_{ev}}\right)^{0.67}\right)\right]^{-2}\right\}^{-0.5} \tag{34}$$

where h_{el} and h_{ev} are the heat transfer coefficient of the liquid-phase and vapor-phase refrigerant, respectively; ρ_{el} and ρ_{ev} are the density of the liquid-phase and vapor-phase refrigerant, respectively; x_e is the vapor quality of the refrigerant.

Fig. 5 depicts the calculation flow chart of the steady-state model of the air-source heat pump. Firstly, the structural parameters of main components model are set. The values of the evaporation pressure (P_e) and condensation pressure (P_c) are assumed. Then, the compressor model, condenser model, and expansion valve will be operated in order. The difference between the mass flow rate of the refrigerant in the compressor (m_c) and the mass flow rate of the refrigerant in the expansion valve (m_v) will be judged. If this difference cannot be accepted, the P_c will be changed. The P_c will be increased when the m_c is larger than m_v, and vice versa. Once the difference is acceptable, the evaporator model will be operated. Next, the difference between the heat transfer rate in the condenser (Q_c) and the sum of the heat transfer rate in the evaporator (Q_e) and power of the compressor (W_c) will be judged. If this difference cannot be accepted, the P_e will be changed. The P_e will be increased when the Q_c is less than the sum of Q_e and W_c. Once the difference is acceptable, the values of the output variables including Q_c and W_c will be obtained. The relationship between the Q_c and the given water flow rate (m_w), and that between the W_c and the m_w will be identified.

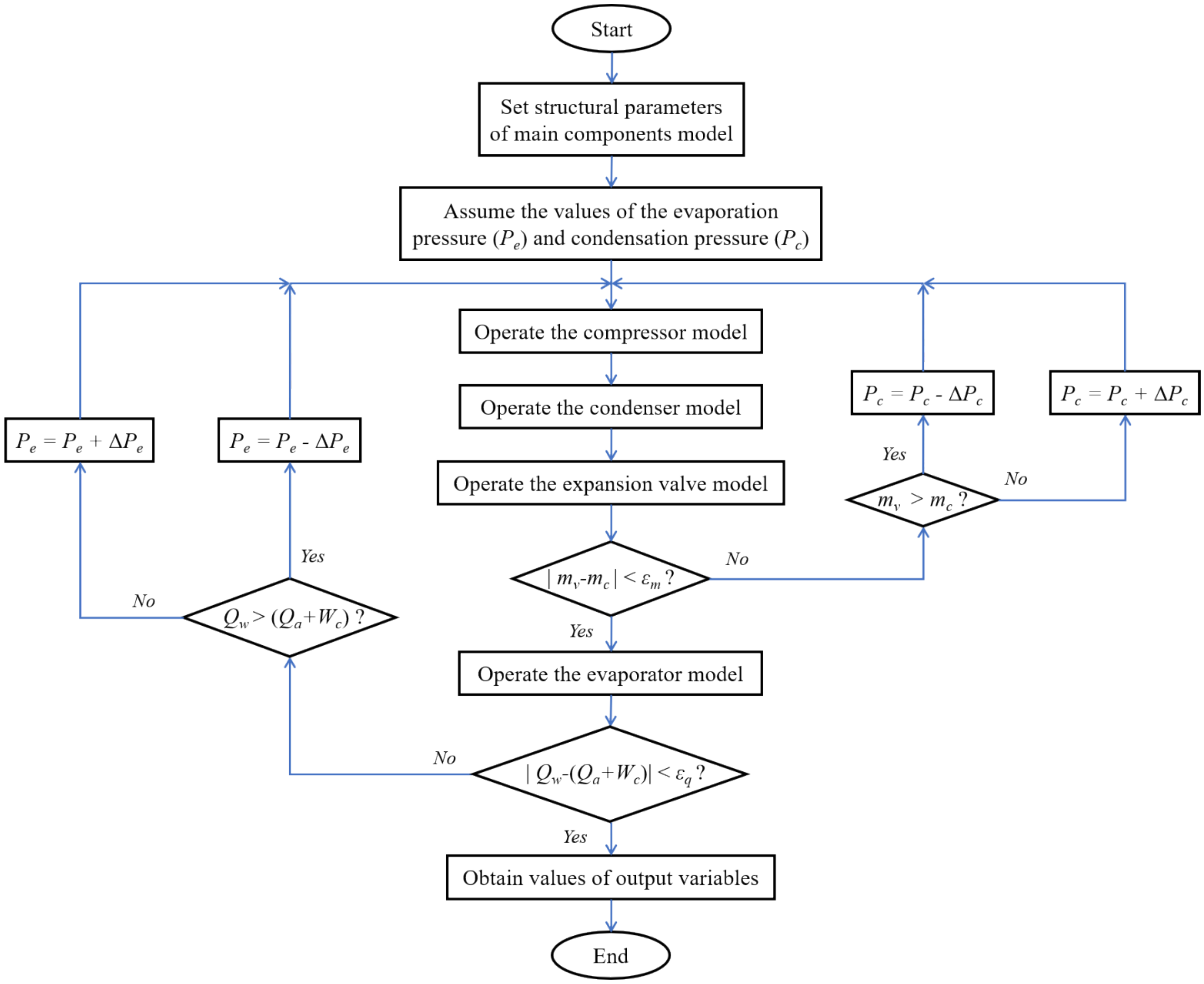

Fig. 5. Calculation flow chart of air-source heat pump model in MATLAB.

(b) TRNSYS model

The schematic for the adopted air-source heat pump model in TRNSYS is shown in Fig. 6. The inputs are the inlet water temperature and the water flowrate; while the outputs are the outlet water temperature and the power.

The outlet water temperature of the air-source heat pump ($T_{o,w}$) is calculated by Eqn. (35):

$$T_{o,w}(t) = T_{i,w}(t) + \frac{q_{hp,act}}{c_w m_w} \tag{35}$$

where $q_{hp,act}$ is the actual heat transfer rate of the air-source heat pump, which is determined by Eqn. (36):

$$q_{hp,act}(t) = \varphi_{hp,q}(t) q_{hp,rated} \tag{36}$$

where $\varphi_{hp,q}$ is a correction factor of the heat transfer rate; and $q_{hp,\,rated}$ is the rated heating capacity of the air-source heat pump. The actual power of the air-source heat pump ($P_{hp,act}$) is determined by Eqn. (37):

$$P_{hp,act}(t) = \varphi_{hp,P}(t)P_{hp,\,rated} \tag{37}$$

where $\varphi_{hp,p}$ is a correction factor of the actual power; and $P_{hp,\,rated}$ is the rated power of the air-source heat pump.

The correction factors $\varphi_{hp,q}$ and $\varphi_{hp,p}$ are normally nonlinear functions of the inlet water temperature and flowrate as well as the outdoor dry bulb temperature. Their values are derived from the data generated by the stead-state model of the air-source heat pump.

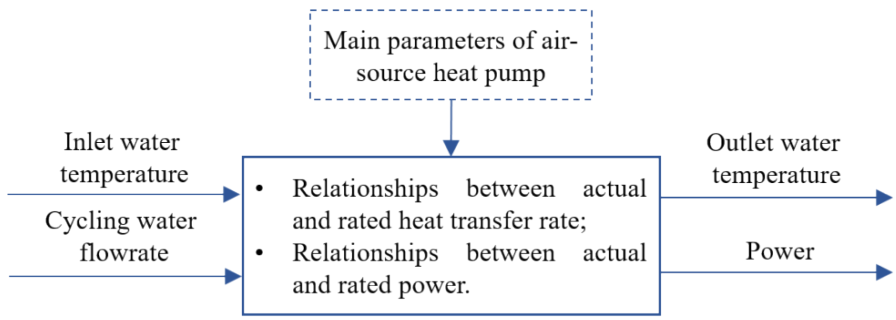

Fig. 6. Schematic diagram of air-source heat pump model in TRNSYS.

2.3.2 PCM storage tank

The schematic of the adopted PCM storage tank model is shown in Fig. 7. The inputs are the inlet water temperature and the water flowrate; while the outputs are the outlet water temperature. Fig. 8 shows the schematic diagram of the heat transfer process between the PCM and the water inside the storage tank. To simplify the thermodynamic model of the PCM storage tank, the following assumptions are made [41]:

- The temperature of the PCM is invariable during the change process;
- No heat transfer occurs between the storage tank and the ambient environment;
- Only the temperature variation of the PCM and the water along the water flow direction is considered;
- The thermo-physical properties of the PCM and the water are not affected by the temperature.

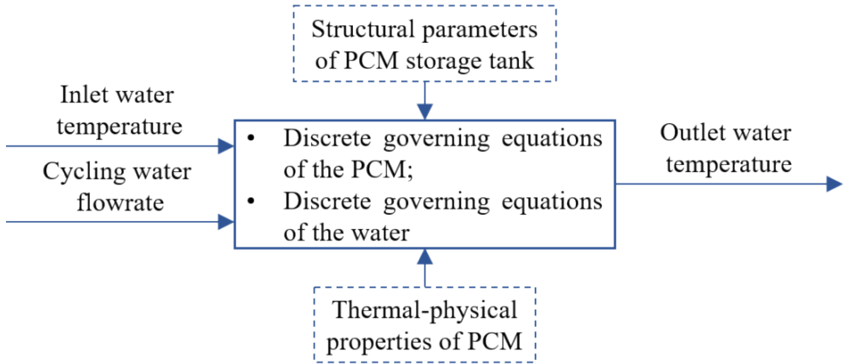

Fig. 7. Schematic diagram of PCM storage tank model.

Based on the above assumptions, the governing energy balance equation of the heat transfer process between the PCM and the water is calculated by Eqn. (38):

$$\rho_{wr} cp_{wr} \varepsilon_{wr} \left(\frac{\partial T_{wr}}{\partial t} + v_{wr} \frac{\partial T_{wr}}{\partial x}\right) = k_{wr} \varepsilon_{wr} \frac{\partial^2 T_{wr}}{\partial^2 x} + \frac{h_t A_{pm} (T_{pm} - T_{wr})}{V_e} \quad (38)$$

where ρ_{wr}, cp_{wr}, v_{wr}, T_{wr}, and k_{wr} are the density, specific heat, velocity, temperature, and thermal conductivity of the water, respectively; t is the time; ε_{wr} is the water fraction in the energy storage tank; h_t is the effective convective heat transfer coefficient between the water and the PCM; A_{pm} is the heat transfer area of the tube wall; T_{pm} is the temperature of the PCM; V_e is the volume of one element; and x is the distance along the water flow direction.

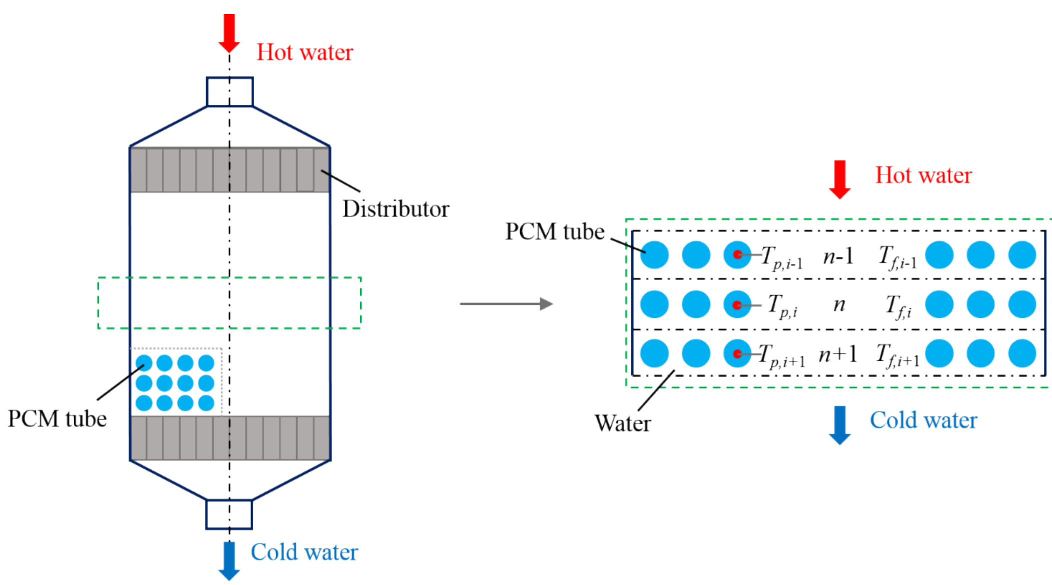

Fig. 8. Schematic diagram of the heat transfer process between the PCM and HTF in the storage tank ("n" represents the number of the row; and "i" represents the number of the divided volume for the PCM or water).

The heat transfer of the PCM is determined by Eqn. (39):

$$\rho_{pm}(1-\varepsilon_{wr})\frac{\partial H_{pm}}{\partial t}=\frac{h_t A_{pm}(T_{pm}-T_{wr})}{V_e} \tag{39}$$

where ρ_{pm} and H_{pm} are the density and enthalpy of the PCM, respectively. H_{pm} is calculated by Eqn. (40):

$$H_{pm}=cp_{pm}T_{pm}+f_m\Delta H_{pm} \tag{40}$$

where cp_{pm} is the specific heat of the PCM; ΔH_{pm} is the melting latent heat of the PCM; and f_m is the melting fraction of the PCM, which is determined by Eqn. (41):

$$\begin{cases} f_m=0, & T_{pm}< T_m \\ 0<f_m<1, & T_{pm}= T_m \\ f_m=1, & T_{pm}> T_m \end{cases} \tag{41}$$

where T_m is the melting point temperature of the PCM.

The convective heat transfer coefficient of the water (h_{wr}) is calculated by Eqn. (42) [42]:

$$h_{wr}=\frac{k_{wr}Nu_{wr}}{D_{out}} \tag{42}$$

where Nu_{wr} is the Nussle number of the water, given by Eqn. (43):

$$Nu_{wr}=BRe_{wr}^{z}Pr_{wr}^{1/3} \tag{43}$$

where Re_{wr} and Pr_{wr} are the Reynolds and Prandtl numbers of the water, respectively; and B and z are coefficients, which can be identified according to the range of Re_{wr}.

3. Case study

3.1. Parameters of PCM storage tank

The paraffin wax is used as the PCM, the thermal properties of which is presented in Table 1. It has the melting temperature and latent heat of 44°C and 174.12kJ/kg, respectively [43]. The structural parameters of the PCM storage tank are shown in Table 2. The tube outer diameter is 12.7mm [44], and the water fraction is 0.4 [45].

Table 1 Thermal properties of the paraffin wax [43]

Item	Unit	Values
Melting temperature	(°C)	44

Latent heat	(kJ/kg)	174.12
Thermal conductivity	(W/m·°C)	0.13
Solid density	(kg/m^3)	830
Liquid density	(kg/m^3)	783
Solid specific heat	(kJ/kg·°C)	2.44
Liquid specific heat	(kJ/kg·°C)	2.53

Table 2 Structural parameters of the PCM storage tank

Items	Unit	Values
Column number of PCM tubes	-	5
Row number of PCM tubes	-	25
Tube length	cm	30
Tube inner diameter	mm	12.5
Tube outer diameter	mm	12.7
Water fraction	-	0.4

3.2. Parameters of air-source heat pump

The adopted compressor in this study is hermetically sealed. Its displacement volume is 8.85 cm^3. The rational velocity is 2800 per minute when the electrical frequency is 50 Hz; and it is 3400 per minute when the electrical frequency is 60 Hz. The relationship between the volumetric efficiency (η_{cv}) and the division between the condensation pressure and evaporation pressure (P_c/P_e), and the relationship between the isentropic efficiency (η_{is}) and the P_c/P_e is identified by the measured data from the application specifications of the air-source heat pump. Fig. 9 depicts the relationship between (a) η_{cv} and P_c/P_e; and (b) η_{is} and P_c/P_e.

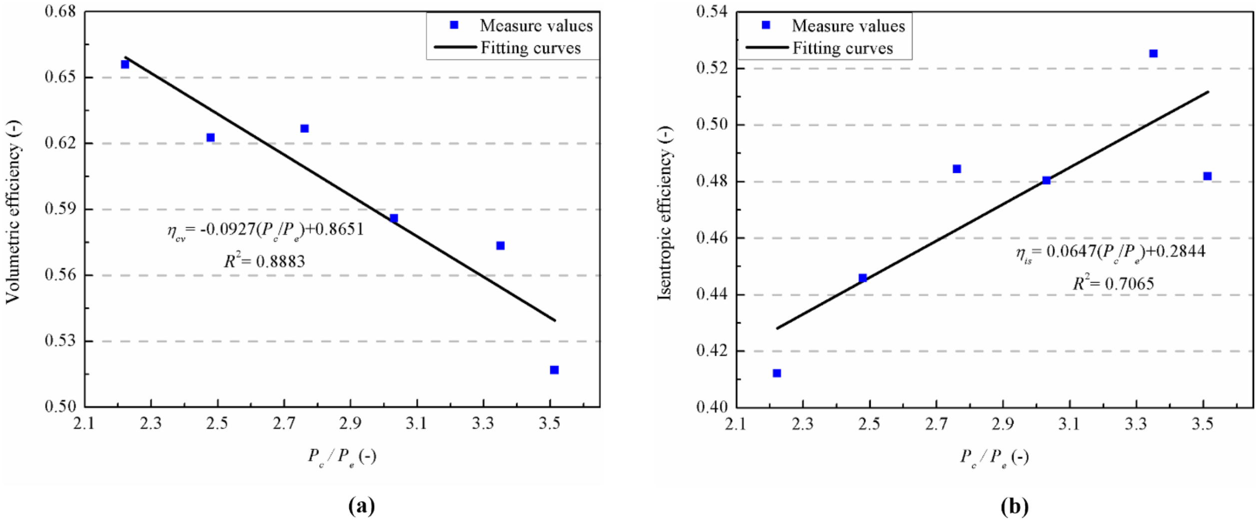

Fig. 9. Relationships between (a) η_{cv} and P_c/P_e; and (b) η_{is} and P_c/P_e.

The relationship between η_{cv} and P_c/P_e can be expressed by Eqn. (44):

$$\eta_{cv} =- 0.0927\left(\frac{P_c}{P_e}\right) + 0.8651 \qquad R^2 = 0.8883 \tag{44}$$

The relationship between η_{is} and P_c/P_e can be expressed by Eqn. (45):

$$\eta_{is} = 0.0647\left(\frac{P_c}{P_e}\right) + 0.2844 \qquad R^2 = 0.7065 \tag{45}$$

The condenser is a plate heat exchanger with the dimension of 14.5cm × 7.6cm × 31.7cm is adopted in this air-source heat pump. The number of the plates is 60, and the corrugation angle is assumed to be 30°. The thickness of the plate is assumed to be 0.5mm [46]. The inlet diameter of the expansion valve is 9.525mm, and the valve opening of 20% is assumed. The finned-tube evaporator with the dimension of 11cm × 29.3cm × 30.5cm is adopted in this air-source heat pump. The total length and diameter of the tubes to be used to transfer heat are 7.032m and 1.02cm. The fin spacing, thickness, and height are 5mm, 0.24mm and 3.5mm, respectively.

3.3. Experimental setup of air-source heat pump

A test rig of an air-source heat pump was built to collect the field data, which is used to validate the reliability of the steady-state model. The main components of the test rig include an air-source heat pump, a water pump, a data logger, three temperature probes, a power meter, a frequency converter and one computer. The experimental air-source heat pump was manufactured by the P.

A. Hilton Ltd. R134a is adopted as the refrigerant in the air-source heat pump. Table 3 shows the information of other main devices used in the experimental process. The temperature probes and data logger were used to collect and record the water and ambient air temperature, respectively. The frequency converter was utilized to maintain the water flow rate at the set value. The power meter was adapted to measure the power of the air-source heat pump.

Table 3 Information of other main devices used in the experiments

Device items	Type	Accuracy	Manufactures
Date logger	BTM-4208SD	≤±0.1%	LUTRON ELECTRONIC ENTERPRISE Co. Ltd.
Temperature probe	K-type	≤±0.4°C	LUTRON ELECTRONIC ENTERPRISE Co. Ltd.
Pump	PT416916	-	FLOJET Co. Ltd.
Power meter	43B	≤±2%	FLUKE Co. Ltd.
Frequency converter	0.75KW/220V	-	Hengxing Xin Co. Ltd.

3.4. Simulation platform

The simulation platform of the charging system was constructed using TRNSYS 17 and MATLAB. Type 941 and Type 3b in the TRNSYS were used to simulate the air-source heat pump and the water pump, respectively. Eqn. (4) was used to describe the relationship between the pump power and the water mass flowrate, where c_0, c_1, c_2, and c_3, was set to be 0, 0.0016, -0.0037, and 0.9671, respectively [32]. The PCM storage tank model presented in the section 2.3 was used in this platform. A finite difference method (FDM) was used to discretize the governing equations [47]; and the discretized algebraic equations were solved by MATLAB codes. The MATLAB codes were linked to TRNSYS 17 using the MATLAB interface Type 155. Fig. 10 presents the established simulation platform.

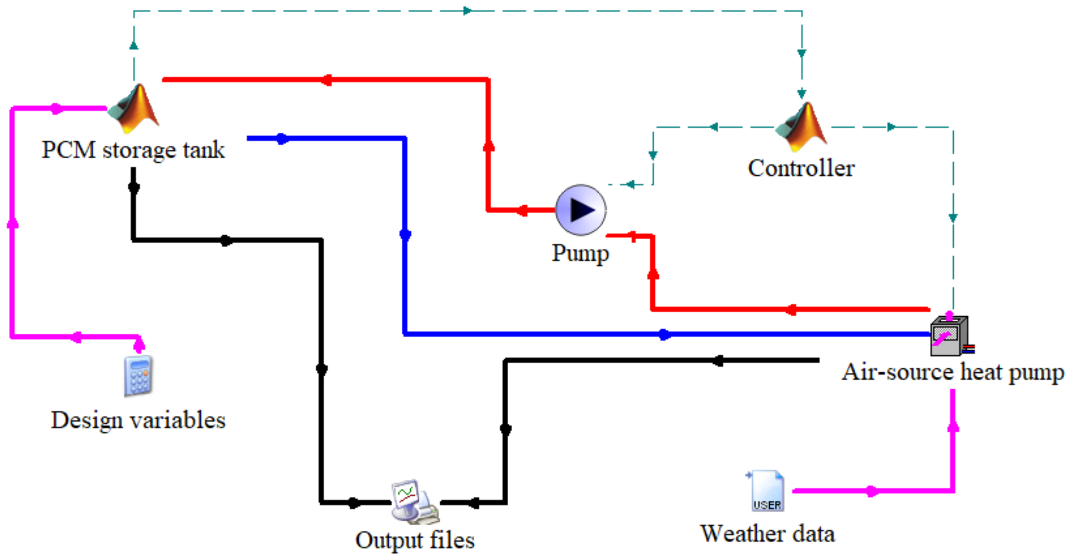

Fig. 10. Established simulation platform in the TRNSYS 17.

4. Results and analysis

4.1. Identification of correction factors

In order to establish the air-source heat pump model in TRNSYS, the correction factors of the heating capacity and power are required to be determined based on the data generated from the steady-state model. The rated heating capacity and power of the air-source heat pump are set to be 1000W and 300W, respectively. Fig. 11 shows the correction factors of the heating capacity, correction factors of the power and the COP of the air-source heat pumps in different water mass flow rate. The ambient air temperature is set to be 20°C. The selected inlet temperature values include 20°C, 25°C, 30°C, 35°C, 40°C, 45°C, 50°C, and 55°C. According to the introduction in the specifications for the air-source heat pump of P. A. Hilton Ltd., the maximum outlet temperature of the air-source heat pump is not more than 55°C. During the simulation process of the steady-state model, 5°C is selected as the safe temperature difference. The typical inlet water temperature values will not be considered when the outlet temperature is more than 60°C. Hence, the selected maximum inlet temperature values when the mass flow rate is 10g/s, 20g/s, 30g/s, 40g/s, and 50g/s are respectively 40°C, 50°C, 55°C, 55°C, and 55°C, as depicted in Fig. 11.

In Fig. 11 (a), the correction factor of the heating capacity reduces with the increase of the inlet temperature, and with the decrease of the mass flow rate. The maximum correction factors when the mass flow rate is 10g/s, 20g/s, 30g/s, 40g/s, and 50g/s are 0.924, 0.944, 0.951, 0.964, and 0.964, respectively; and the minimum correction factors when the mass flow rate is 10g/s, 20g/s, 30g/s, 40g/s, and 50g/s are 0.726, 0.800, 0.800, 0.815, and 0.815, respectively. In Fig. 11 (b), the correction factor of the power increases with the increase of the inlet temperature, and with the decrease of the mass flow rate. The maximum correction factors when the mass flow rate is 10g/s, 20g/s, 30g/s, 40g/s, and 50g/s are 1.920, 1.869, 1.977, 1.950, and 1.900, respectively; and the minimum correction factors when the mass flow rate is 10g/s, 20g/s, 30g/s, 40g/s, and 50g/s are 1.369, 1.061, 1.028, 0.992, and 0.964, respectively. In Fig. 11 (c), the COP of the air-source heat pump reduces with the increase of the inlet temperature, and with the decrease of the mass flow rate. The maximum COP when the mass flow rate is 10g/s, 20g/s, 30g/s, 40g/s, and 50g/s are 2.25, 2.97, 3.08, 3.24, and 3.40, respectively; and the minimum COP when the mass flow rate is 10g/s, 20g/s, 30g/s, 40g/s, and 50g/s are 1.26, 1.42, 1.34, 1.39, and 1.43, respectively.

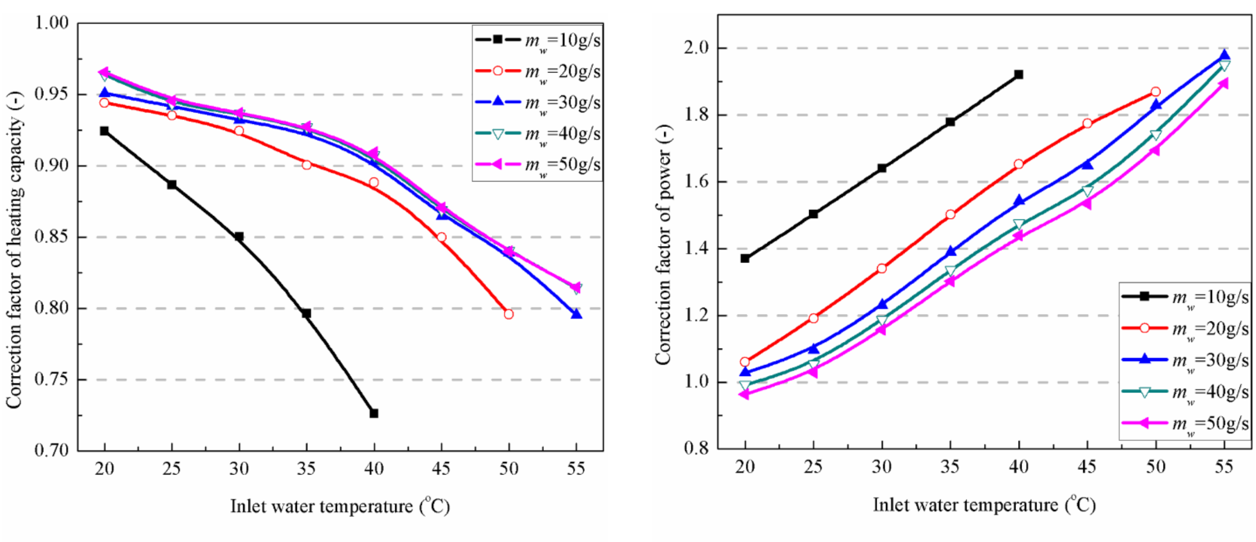

(a) **(b)**

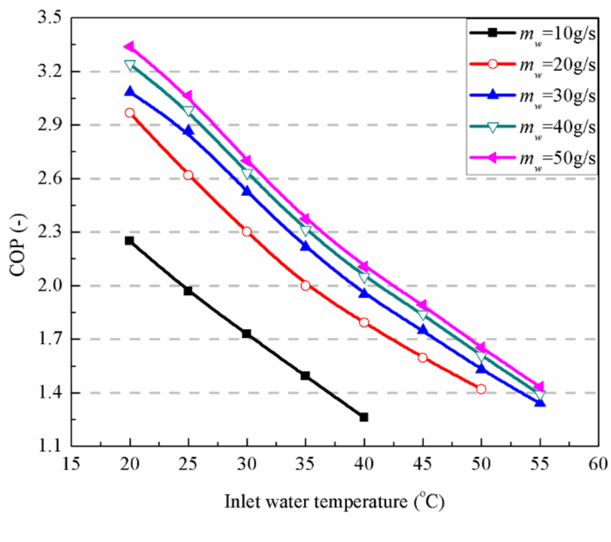

(c)

Fig. 11. (a) Correction factors of heating capacity; (b) correction factors of power; and (c) COP of the air-source heat pump in different water mass flow rate.

4.2. Model validation

To evaluate the correctness and reliability of the adopted models, the average relative error (e_a) between the predicted and measured temperature is selected as the indicator, defined by Eqn. (46):

$$e_a = \frac{1}{s}\sum_{k=1}^{k=s}\left|\frac{M_{exp,k} - M_{sim,k}}{M_{exp,k}}\right| \times 100\% \tag{46}$$

where s is the number of samples; $M_{exp,k}$ and $M_{sim,k}$ are the measured and predicted values, respectively.

In our previous study [14], the correctness and reliability of the dynamic heat transfer model of the PCM storage tank have been validated. The e_a of this model is 3.97%, which suggests that this model is reliable and correct. Fig. 12 depicts the measured values and deviations between the measured and calculated values in different inlet temperature of the air-source heat pump, and the error bands in the measurements were set according to the accuracy of the measuring devices. During the test process, the cycling water mass flowrate was maintained at 44g/s, and the ambient air temperature was around 19°C. The typical water inlet temperature was 25°C, 30°C, 35°C, 40°C, 45°C, 50°C, and 55°C. It can be seen that there was a good agreement between the calculated and measured outlet water temperature. The e_a of outlet water temperature and power was respectively 1.21% and 10.8%, which suggested that the steady-state model of the air-source heat pump was reliable and accurate. Thus, the developed air-source heat pump model in TRNSYS was also reliable, since performance maps were established by the steady-state model in MATLAB.

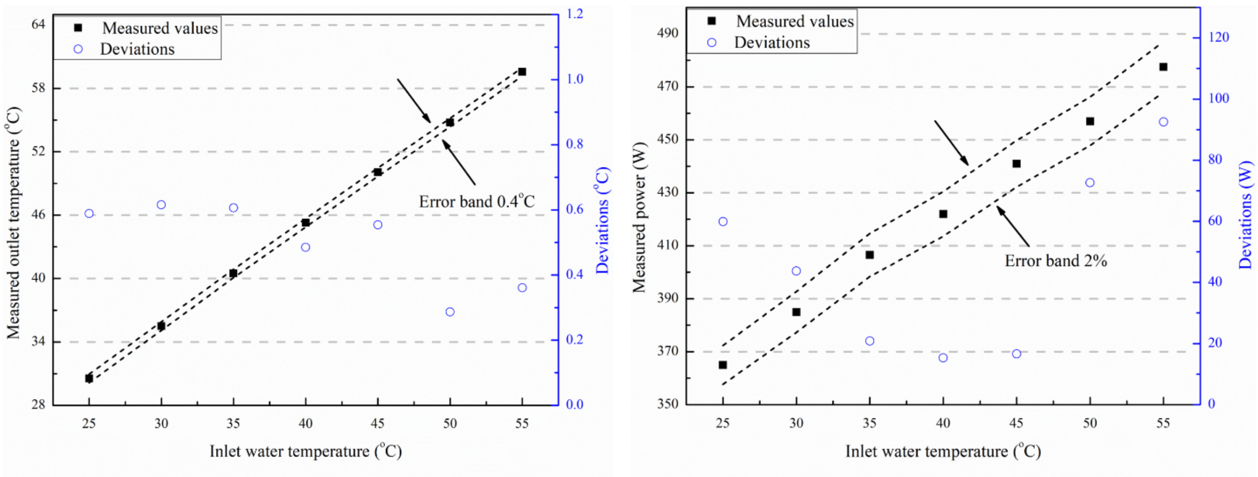

(a) (b)

Fig. 12. Measured values and deviations between the measured and calculated values of (a) outlet temperature and (b) power in different inlet temperature.

4.3. Effect on water temperature variation

The charging process when the ambient air temperature was 20°C, and the initial temperature of the PCM storage tank was 20°C, was simulated. Fig. 13 shows the inlet and outlet temperature variation of the air-source heat pump with time in different water mass flow rate. The charging process was completed when the outlet temperature of the air-source heat pump reached to 55°C, which was the maximum water temperature the air-source heat pump could heat up to. Except the case when the mass flow rate was 10g/s, other cases experienced a period with relatively steady temperature variation, due to the occurrence of the phase change process. The lower mass flow rate lead to the higher outlet temperature, resulting from higher temperature difference between inlet and outlet water temperature. Although the inlet temperature of the PCM storage tank (i.e. outlet temperature of the air-source heat pump) increased with the decrease of the water mass flow rate, the outlet temperature of the PCM storage tank (i.e. inlet temperature of the air-source heat pump) increased with the increase of the water flow rate. The reason might be that the higher water mass flow rate results in the higher heat transfer rate in the air-source heat pump.

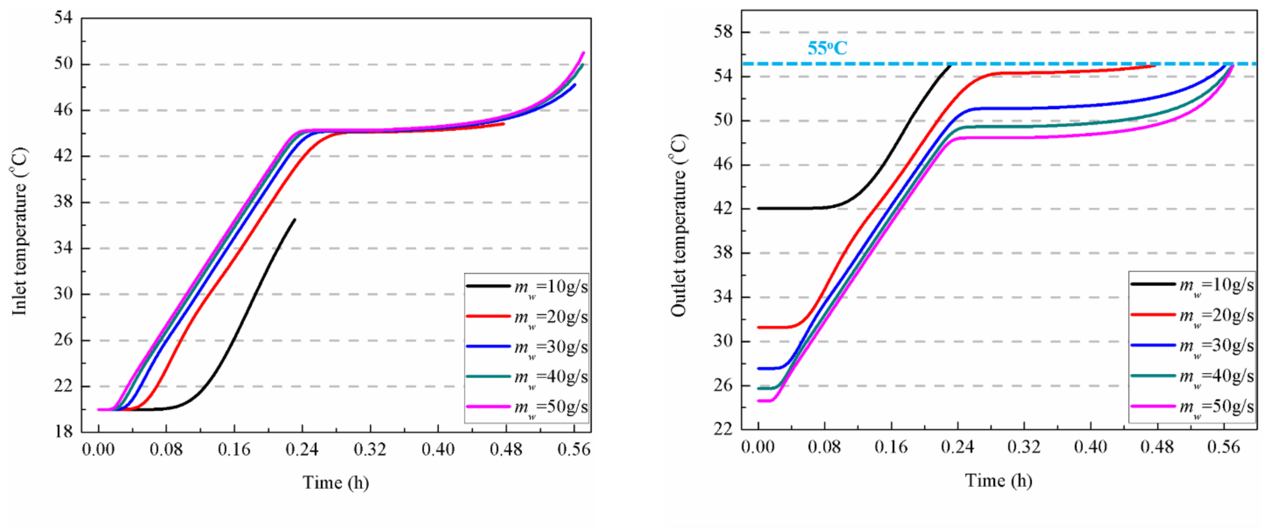

(a) **(b)**

Fig. 13. Variation of (a) inlet temperature and (b) outlet temperature of the air-source heat pump with time in different water mass flow rate.

4.4. Effect on charging time

Fig. 14 depicts the variation of the charging time with water mass flow rate in different stored heat energy. When the required stored heat energy is fixed, the charging time reduces with the increase of the water mass flow rate. For example, as shown in Fig. 14 (b), the charging time is 659.4s, 644.3s, 639.9s, 637.2s, and 637.2s, when the water mass flow rate is 10g/s, 20g/s, 30g/s, 40g/s, and 50g/s, respectively. The relationships between the charging time (t_c) and the mass flow rate (m_w) in different stored heat energy (E_{stored}) are summarized in Table 4.

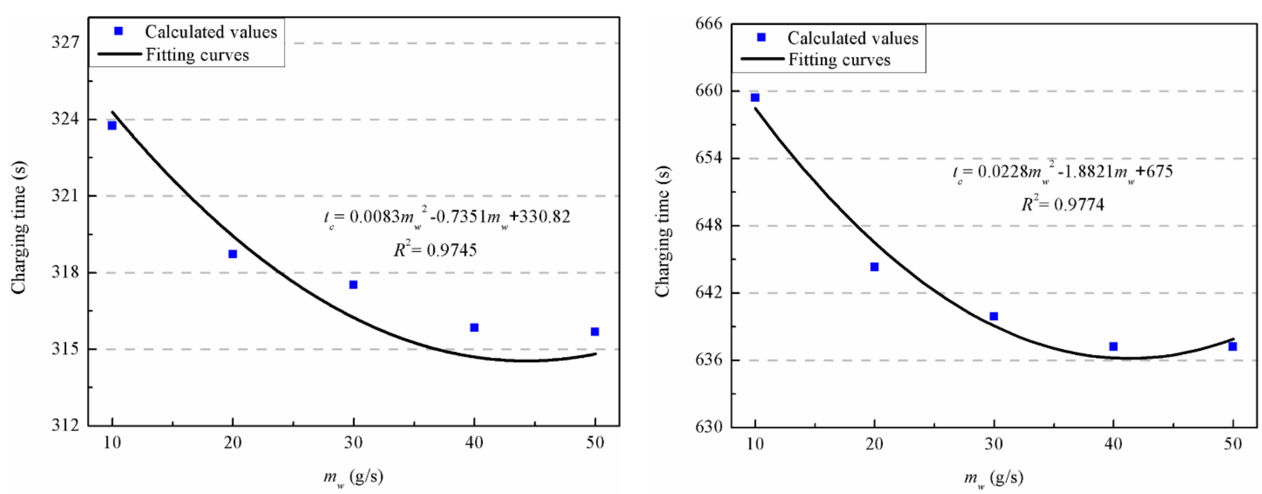

(a) E_{stored} = 300kJ **(b)** E_{stored} = 600kJ

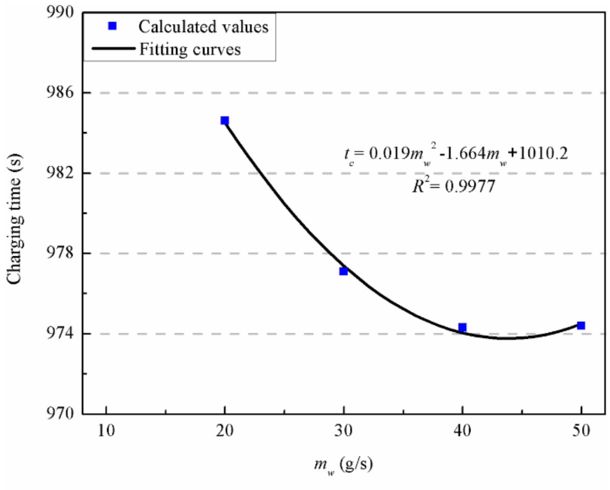

(c) E_{stored} = 900kJ

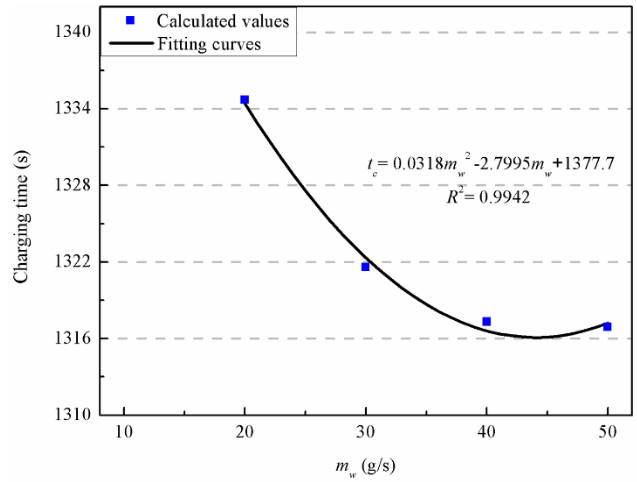

(d) E_{stored} = 1200kJ

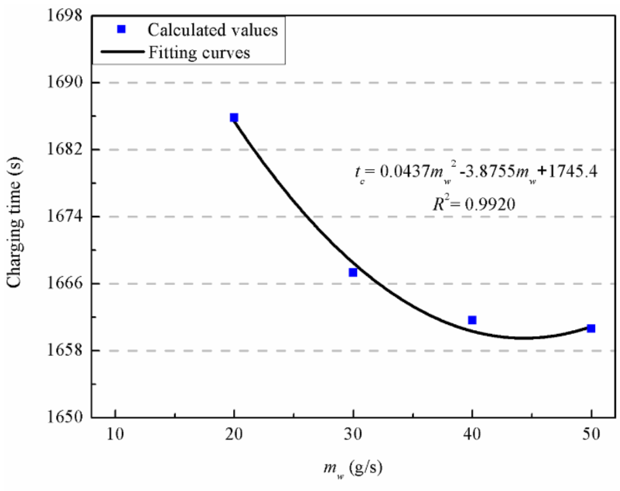

(e) E_{stored} = 1500kJ

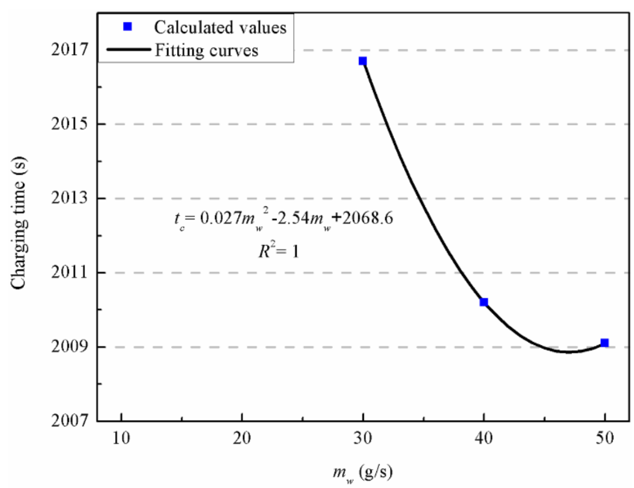

(f) E_{stored} = 1800kJ

Fig. 14. Variation of charging time with water mass flow rate in different stored heat energy: (a) 300kJ; (b) 600kJ; (c) 900kJ; (d) 1200kJ; (e) 1500kJ; and (f) 1800kJ.

Table 4 The relationships between the t_c and m_w in different E_{stored}

E_{stored}	Relationships between t_c and m_w	
300 kJ	$t_c = 0.0083{m_w}^2 - 0.7351m_w + 330.82$	$R^2 = 0.9745$
600 kJ	$t_c = 0.0228{m_w}^2 - 1.8821m_w + 675$	$R^2 = 0.9774$
900 kJ	$t_c = 0.019{m_w}^2 - 1.664m_w + 1010.2$	$R^2 = 0.9977$
1200 kJ	$t_c = 0.0318{m_w}^2 - 2.7995m_w + 1377.7$	$R^2 = 0.9942$
1500 kJ	$t_c = 0.0437{m_w}^2 - 3.8755m_w + 1745.4$	$R^2 = 0.9920$
1800 kJ	$t_c = 0.027{m_w}^2 - 2.54m_w + 2068.6$	$R^2 = 1$

4.5. Effect on total energy use

Fig. 15 shows the variation of total energy use with water flow rate in different stored heat energy: (a) 300kJ; (b) 600kJ; (c) 900kJ; (d) 1200kJ; (e) 1500kJ; and (f) 1800kJ. From Fig. 15 (c), (d), and (e), it could be seen that the case when the mass flow rate was 10g/s, cannot satisfy the stored heat energy demand of 900kJ, 1200kJ, and 1500kJ. From Fig. 15 (f), it could be seen that the cases when the mass flow rate was 10g/s and 20g/s, cannot satisfy the stored heat energy demand of 1800kJ. For the stored heat energy demand of 300kJ, 600kJ, 900kJ, 1200kJ, 1500kJ, and 1800kJ, the minimum total energy use was 115.4kJ, 256.3kJ, 431.2kJ, 616.1kJ, 802.5kJ, and 996.2kJ, which occurred when the mass flow rate was 20g/s, 30g/s, 30g/s, 30g/s, 30g/s, and 30g/s, respectively. The relationships between the total energy use (E_{total}) and the mass flow rate (m_w) in different stored heat energy (E_{stored}) are summarized in Table 5.

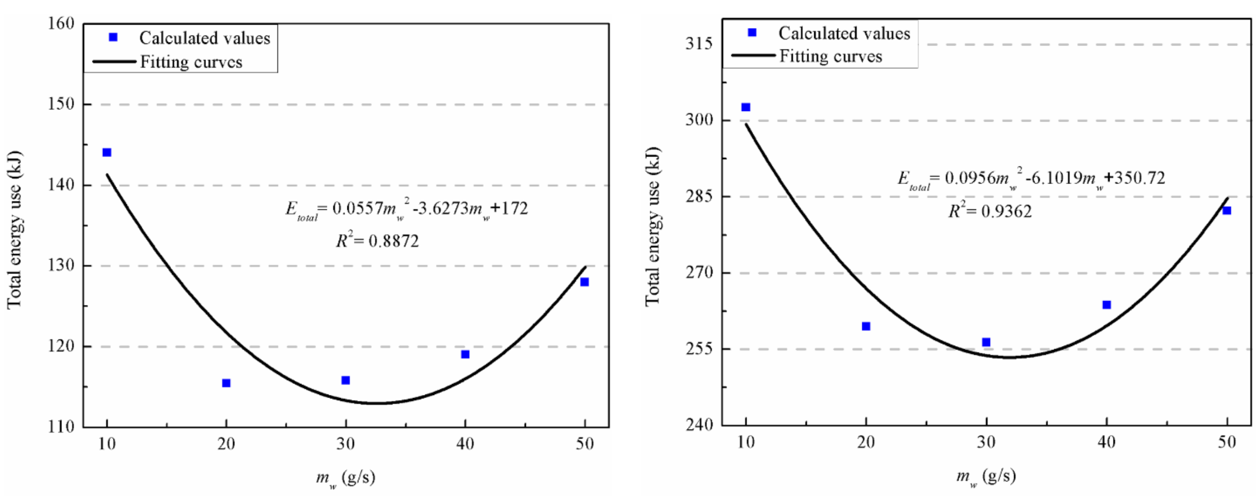

(a) E_{stored} = 300kJ

(b) E_{stored} = 600kJ

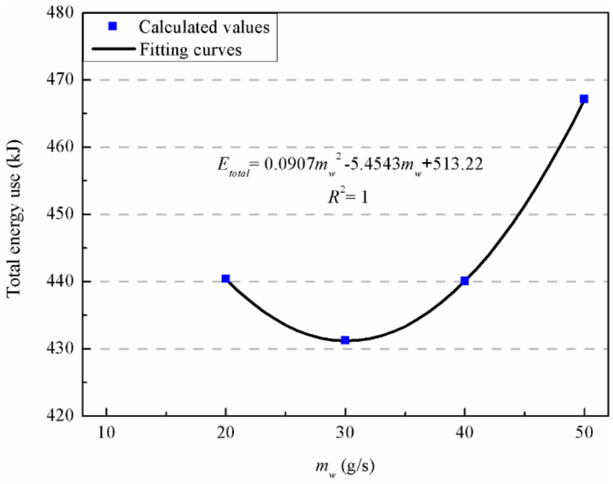

(c) E_{stored} = 900kJ

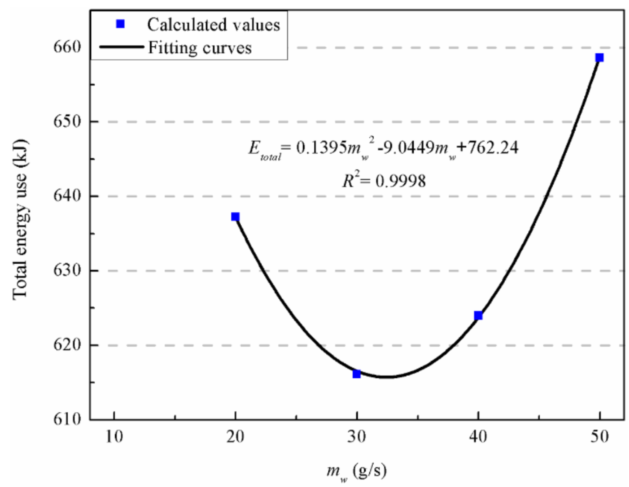

(d) E_{stored} = 1200kJ

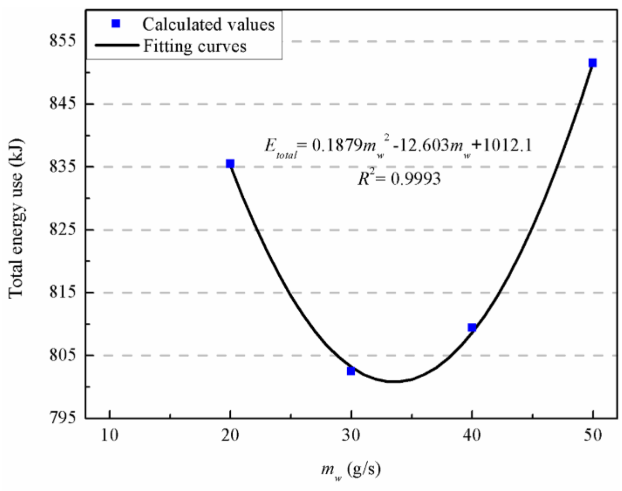

(e) E_{stored} = 1500kJ

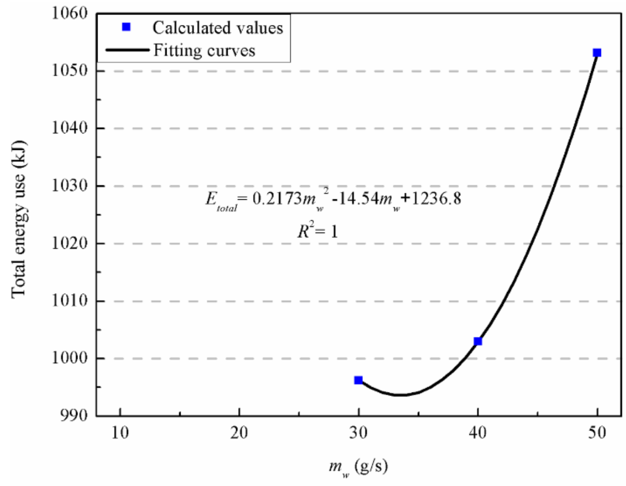

(f) E_{stored} = 1800kJ

Fig. 15. Variation of total energy use with water flow rate in different stored heat energy: (a) 300kJ; (b) 600kJ; (c) 900kJ; (d) 1200kJ; (e) 1500kJ; and (f) 1800kJ.

Table 5 The relationships between the E_{total} and m_w in different E_{stored}

E_{stored}	Relationships between E_{total} and m_w	
300 kJ	$E_{total} = 0.0557{m_w}^2 - 3.6273m_w + 172$	$R^2 = 0.8872$
600 kJ	$E_{total} = 0.0956{m_w}^2 - 6.1019m_w + 350.72$	$R^2 = 0.9362$
900 kJ	$E_{total} = 0.0907{m_w}^2 - 5.4543m_w + 513.22$	$R^2 = 1$
1200 kJ	$E_{total} = 0.1395{m_w}^2 - 9.0449m_w + 762.24$	$R^2 = 0.9998$
1500 kJ	$E_{total} = 0.1879{m_w}^2 - 12.603m_w + 1012.1$	$R^2 = 0.9993$
1800 kJ	$E_{total} = 0.2173{m_w}^2 - 14.54m_w + 1236.8$	$R^2 = 1$

5. Conclusions

In this study, the energy performance of the charging process when an air-source heat pump was used to charge a PCM storage tank was comprehensively investigated. The simulation platform of the system was constructed by TRNSYS and MATLAB. The thermodynamic model of the PCM storage tank has been validated by the previous experimental results in the literature. A steady-state model of the air-source heat pump was solved and validated by measured data from the established experimental setup. The typical values of the input and output variables from the steady-state model were used to identify the required correction factors of the air-source heat pump model in TRNSYS. Based on the established platform, the effect of the water mass flow rate on the inlet and outlet temperature variation, charging time, and total energy in different stored heat energy were analyzed. The increase of the water mass flow rate led to the increase of the inlet temperature of the PCM storage tank, but it led to the decrease of the outlet temperature of the PCM storage tank. The increase of the water mass flow rate led to the decrease of the charging time in the fixed stored heat energy demand. In addition, it was found that in given stored heat energy demand, the relationships between the water mass flow and total energy use could be well fit in a quadratic expression. The optimal water mass flow rate for obtaining the minimum total energy use could be identified by these relationships. Hence, this study presented an efficient analysis method for investigating the energy performance of using the air-source heat pump to charge the PCM storage tank. This method could effectively determine the relationships between the water flow rate and total energy use, which provides a meaningful guideline for the optimal design of the system integrates the air-source heat pumps and PCM storage tank.

Further studies should be conducted as follows: (i) the used air-source heat pump model in TRNSYS is developed based on performance map, which is constructed by steady-state model in MATLAB. More advanced laboratory conditions should be used to obtain huge amount of high-accuracy data for establishing performance map for air-source heat pump model in TRNSYS; (ii) more complex heat transfer model of air-source heat pump should be established for investigating the dynamic behavior of using air-source heat pump to charge PCM storage tank; (iii) more comprehensive experimental platform of the entire system that comprises both air-source heat pump and PCM storage tank should be established, and it can be used for the validation of the dynamic behavior of the entire system (e.g. charging time).

Acknowledgments

The authors sincerely thank the anonymous reviewers for their time and effort. In addition, the authors appreciate the support of Dr. Gongsheng Huang.

References

[1] Vivas FJ, De las Heras A, Segura F, Andújar JM. A review of energy management strategies for renewable hybrid energy systems with hydrogen backup. Renewable and Sustainable Energy Reviews. 2018;82:126-55.

[2] Kousha N, Rahimi M, Pakrouh R, Bahrampoury R. Experimental investigation of phase change in a multitube heat exchanger. Journal of Energy Storage. 2019;23:292-304.

[3] Tian Z, Perers B, Furbo S, Fan J. Annual measured and simulated thermal performance analysis of a hybrid solar district heating plant with flat plate collectors and parabolic trough collectors in series. Applied Energy. 2017;205:417-27.

[4] Du Y, Blocken B, Pirker S. A novel approach to simulate pollutant dispersion in the built environment: Transport-based recurrence CFD. Building and Environment. 2020;170.

[5] Du Y, Mak CM, Li Y. A multi-stage optimization of pedestrian level wind environment and thermal comfort with lift-up design in ideal urban canyons. Sustainable Cities and Society. 2019;46.

[6] Du Y, Mak CM, Li Y. Application of a multi-variable optimization method to determine lift-up design for optimum wind comfort. Building and Environment. 2018;131:242-54.

[7] Liu X, Zhang P, Pimm A, Feng D, Zheng M. Optimal design and operation of PV-battery systems considering the interdependency of heat pumps. Journal of Energy Storage. 2019;23:526-36.

[8] Saydam V, Parsazadeh M, Radeef M, Duan X. Design and experimental analysis of a helical coil phase change heat exchanger for thermal energy storage. Journal of Energy Storage. 2019;21:9-17.

[9] Holma A, Leskinen P, Myllyviita T, Manninen K, Sokka L, Sinkko T, et al. Environmental impacts and risks of the national renewable energy targets – A review and a qualitative case study from Finland. Renewable and Sustainable Energy Reviews. 2018;82:1433-41.

[10] Zhang L, Jiang Y, Dong J, Yao Y. Advances in vapor compression air source heat pump

system in cold regions: A review. Renewable and Sustainable Energy Reviews. 2018;81:353-65.

[11] Zhang Q, Zhang L, Nie J, Li Y. Techno-economic analysis of air source heat pump applied for space heating in northern China. Applied Energy. 2017;207:533-42.

[12] Underwood CP, Shepherd T, Bull SJ, Joyce S. Hybrid thermal storage using coil-encapsulated phase change materials. Energy and Buildings. 2018;159:357-69.

[13] de Gracia A, Cabeza LF. Numerical simulation of a PCM packed bed system: A review. Renewable and Sustainable Energy Reviews. 2017;69:1055-63.

[14] Li Y, Huang G, Xu T, Liu X, Wu H. Optimal design of PCM thermal storage tank and its application for winter available open-air swimming pool. Applied Energy. 2018;209:224-35.

[15] Xu T, Li Y, Chen J, Liu J. Preparation and thermal energy storage properties of LiNO 3 -KCl-NaNO 3 /expanded graphite composite phase change material. Solar Energy Materials and Solar Cells. 2017;169:215-21.

[16] Navarro L, Barreneche C, Castell A, Redpath DAG, Griffiths PW, Cabeza LF. High density polyethylene spheres with PCM for domestic hot water applications: Water tank and laboratory scale study. Journal of Energy Storage. 2017;13:262-7.

[17] Barreneche C, Navarro ME, Cabeza LF, Fernández AI. New database to select phase change materials: Chemical nature, properties, and applications. Journal of Energy Storage. 2015;3:18-24.

[18] Ferrer G, Barreneche C, Solé A, Martorell I, Cabeza LF. New proposed methodology for specific heat capacity determination of materials for thermal energy storage (TES) by DSC. Journal of Energy Storage. 2017;11:1-6.

[19] Zou D, Ma X, Liu X, Zheng P, Cai B, Huang J, et al. Experimental research of an air-source heat pump water heater using water-PCM for heat storage. Applied Energy. 2017;206:784-92.

[20] Kumar GS, Nagarajan D, Chidambaram L, Kumaresan V, Ding Y, Velraj R. Role of PCM addition on stratification behaviour in a thermal storage tank–An experimental study. Energy. 2016;115:1168-78.

[21] Navarro L, Barreneche C, Castell A, Redpath DA, Griffiths PW, Cabeza LF. High density polyethylene spheres with PCM for domestic hot water applications: Water tank and laboratory scale study. Journal of Energy Storage. 2017;13:262-7.

[22] Moreno P, Castell A, Sole C, Zsembinszki G, Cabeza LF. PCM thermal energy storage tanks in heat pump system for space cooling. Energy and Buildings. 2014;82:399-405.

[23] Kumar GS, Nagarajan D, Chidambaram LA, Kumaresan V, Ding Y, Velraj R. Role of PCM

addition on stratification behaviour in a thermal storage tank – An experimental study. Energy. 2016;115:1168-78.
[24] Moreno P, Castell A, Solé C, Zsembinszki G, Cabeza LF. PCM thermal energy storage tanks in heat pump system for space cooling. Energy and Buildings. 2014;82:399-405.
[25] Wang Y, Yang X, Xiong T, Li W, Shah KW. Performance evaluation approach for solar heat storage systems using phase change material. Energy and Buildings. 2017;155:115-27.
[26] Yang L, Zhang X, Xu G. Thermal performance of a solar storage packed bed using spherical capsules filled with PCM having different melting points. Energy and Buildings. 2014;68:639-46.
[27] Elbahjaoui R, Qarnia HE. Thermal performance analysis of combined solar collector with triple concentric-tube latent heat storage systems. Energy and Buildings. 2018.
[28] Cheng X, Zhai X. Thermal performance analysis of a cascaded cold storage unit using multiple PCMs. Energy. 2018;143:448-57.
[29] Wang Y, Wang L, Xie N, Lin X, Chen H. Experimental study on the melting and solidification behavior of erythritol in a vertical shell-and-tube latent heat thermal storage unit. International Journal of Heat and Mass Transfer. 2016;99:770-81.
[30] Tao Y, Liu Y, He Y-L. Effects of PCM arrangement and natural convection on charging and discharging performance of shell-and-tube LHS unit. International Journal of Heat and Mass Transfer. 2017;115:99-107.
[31] Wu S, Fang G, Liu X. Thermal performance simulations of a packed bed cool thermal energy storage system using n-tetradecane as phase change material. International Journal of Thermal Sciences. 2010;49:1752-62.
[32] Wan H, Xu X, Li A, Yan T, Gang W. A wet-bulb temperature-based control method for controlling the heat balance of the ground soil of a hybrid ground-source heat pump system. Advances in Mechanical Engineering. 2017;9.
[33] Underwood CP, Royapoor M, Sturm B. Parametric modelling of domestic air-source heat pumps. Energy and Buildings. 2017;139:578-89.
[34] Xia ZZ, Yang GZ, Wang RZ. Experimental investigation of capillary-assisted evaporation on the outside surface of horizontal tubes. International Journal of Heat and Mass Transfer. 2008;51:4047-54.
[35] Kong XQ, Zhang D, Li Y, Yang QM. Thermal performance analysis of a direct-expansion solar-assisted heat pump water heater. Energy. 2011.

[36] Mota FA, Carvalho E, Ravagnani MA. Modeling and Design of Plate Heat Exchanger. Heat Transfer: Studies and Applications. 2015:165.

[37] Dalkilic A, Wongwises S. Two-phase heat transfer coefficients of R134a condensation in vertical downward flow at high mass flux. Heat Transfer-Theoretical Analysis, Experimental Investigations and Industrial Systems. 2011:15-32.

[38] Eames IW, Milazzo A, Maidment GG. Modelling thermostatic expansion valves. International Journal of Refrigeration. 2014;38:189-97.

[39] Chen W, Liang S, Guo Y, Cheng K, Gui X, Tang D. Investigation on the thermal performance and optimization of a heat pump water heater assisted by shower waste water. Energy and Buildings. 2013;64:172-81.

[40] Deng W, Yu J. Simulation analysis on dynamic performance of a combined solar/air dual source heat pump water heater. Energy Conversion and Management. 2016;120:378-87.

[41] Li Y, Huang G, Wu H, Xu T. Feasibility study of a PCM storage tank integrated heating system for outdoor swimming pools during the winter season. Applied Thermal Engineering. 2018;134:490-500.

[42] Yang S-M, Tao W-Q. Heat transfer theory. Beijing: People. 2006.

[43] Hasan MI, Basher HO, Shdhan AO. Experimental investigation of phase change materials for insulation of residential buildings. Sustainable cities and society. 2018;36:42-58.

[44] Dadollahi M, Mehrpooya M. Modeling and investigation of high temperature phase change materials (PCM) in different storage tank configurations. Journal of Cleaner Production. 2017;161:831-9.

[45] Peng H, Dong H, Ling X. Thermal investigation of PCM-based high temperature thermal energy storage in packed bed. Energy conversion and management. 2014;81:420-7.

[46] Anusha G, Kishore P. Heat Transfer Analysis of Gasketed Plate Heat Exchanger. A A. 2017;1:1p.

[47] Wu S, Fang G. Dynamic performances of solar heat storage system with packed bed using myristic acid as phase change material. Energy and Buildings. 2011;43:1091-6.